Electronic Supporting Information (ESI) for

A MOF-Derived Co_3O_4/Ni-Co Sulphide Heterojunction for Ultra-Stable Sulphur Oxidation

Yang Chen,[a] Siran Yan,[a] Jing Zhang,[a] Jiayu Gong,[a] Shoudong Xu,*[a] Jiaqi Chen,[a] Ding Zhang,[b] and Liang Chen*[a]

[a] College of Chemical Engineering and Technology, Taiyuan University of Technology, Taiyuan 030024, P. R. China.

[b] School of Chemical Engineering and Pharmacy, Wuhan Institute of Technology, Wuhan 430205, P. R. China.

Experimental Section

Materials and Chemicals.

All the chemicals were of analytical grade and used as received without further purification. Cobalt nitrate hexahydrate ($Co(NO_3)_2 \cdot 6H_2O$, 98%), nickel nitrate hexahydrate ($Ni(NO_3)_2 \cdot 6H_2O$, 98%), sodium sulfide hydrate ($Na_2S \cdot 9H_2O$, 98%), and sodium hydroxide (NaOH, 98%) were purchased from Shanghai Aladdin Biochemical Technology Co., Ltd. 2-Methylimidazole (2-MIM, $C_4H_6N_2$, 98%) and thiourea (CH_4N_2S, 99%) were obtained from Shanghai Macklin Biochemical Co., Ltd. Commercial nickel foam (NF) (surface mass density: 350 g m^{-2}, thickness: 1.6 mm) served as the conductive substrate.

Synthesis of precursors of Co_3O_4/NF.

The Co_3O_4 nanosheet arrays were synthesized via a template-assisted strategy using Co-ZIF-L precursor. Initially, the nickel foam (NF) was pretreated by ultrasonication in 1 M HCl for 15 min to remove the intrinsic surface oxide layer, followed by repeated rinsing with deionized (DI) water and alcohol to ensure a pristine surface. The substrate was then dried in a vacuum oven at 55 °C for 6 h.

In a typical synthesis, an aqueous solution of 2-methylimidazole (2-MIM, 1.58 g dissolved in 40 mL DI water) was rapidly poured into an aqueous solution of $Co(NO_3)_2 \cdot 6H_2O$ (0.58 g dissolved in 40 mL DI water). A piece of pretreated NF (2 cm × 3 cm) was immediately immersed into

this reaction mixture and maintained at room temperature for 6 h to facilitate the in-situ vertical growth of Co-ZIF-L nanosheets. Following the reaction, the NF substrate covered with the Co-ZIF-L precursor was rinsed thoroughly with DI water and ethanol to remove unreacted species and then dried in a vacuum oven at 70 °C for 6 h. The dried precursor was subsequently calcined in a muffle furnace at 350 °C for 2 h in an air atmosphere with a heating rate of 3 °C min^{-1}, to obtained the Co_3O_4/NF electrode.

Synthesis of Co_3O_4/NCS/NF.

Nickel-cobalt sulfides (NCS) were deposited onto the Co_3O_4 nanosheet arrays using a typical electrodeposition method. The electrochemical deposition was conducted in a standard three-electrode cell containing 30 mL of electrolyte solution composed of 5 mM $Co(NO_3)_2 \cdot 6H_2O$, 5 mM $Ni(NO_3)_2 \cdot 6H_2O$, and 0.5 M thiourea. A platinum foil and a saturated calomel electrode (SCE) served as the counter and reference electrodes, respectively, with the prepared Co_3O_4/NF acting as the working electrode. Electrodeposition was performed using cyclic voltammetry (CV) for 20 cycles within a potential window of −1.2 V to 0.2 V *vs*. SCE at a scan rate of 10 mV s^{-1}. During the cathodic scan, metal ions (Ni^{2+}, Co^{2+}) and sulfur precursors were co-reduced onto the Co_3O_4 surface. After electrodeposition, the substrate was carefully removed, rinsed thoroughly with DI water and ethanol, briefly sonicated in ethanol to remove loosely

bound particles, and dried in a vacuum oven at 70 °C. For comparison, NCS/NF was also prepared with the same approach with a bare NF instead of the Co_3O_4/NF electrode.

Material characterization.

Powder X-ray diffraction (XRD) analysis was performed using a Bruker D8 Advance powder diffractometer equipped with Cu Kα X-ray radiation (λ = 1.5406 Å). Scanning electron microscopy (SEM) images were acquired by ZEISS Gemini 300 and ZEISS Sigma 360. Transmission electron microscopy (TEM) and high-resolution transmission electron microscopy (HRTEM) images were obtained with a FEI Talos F200X instrument. X-ray photoelectron spectroscopy (XPS) spectra were collected using a Thermo Scientific K-Alpha X-ray photoelectron spectrometer. The shift of the binding energy was corrected using C 1s as an internal standard at 284.8 eV. The UV-Vis spectroscopy was recorded on a UV-5200 (Metash) instrument.

Electrochemical measurements.

All electrochemical measurements were performed on a Corrtest CS3104 multichannel electrochemical workstation. The as-prepared catalysts on NF samples served directly as the working electrode. And the electrode geometric surface area used for current density normalization was 1 cm^2. A graphite rod was used as the counter electrode. Potentials were measured against a Hg/HgO reference electrode (in 1 M NaOH) and

converted to the Reversible Hydrogen Electrode (RHE) scale according to the Nernst equation:

$$E\ (vs.\ \text{RHE}) = E\ (vs.\ \text{Hg/HgO}) + 0.059\ \text{V} \times \text{pH} + 0.098\ \text{V}$$

Where 0.098 V is the standard potential of Hg/HgO *vs*. SHE at 25 °C. In this work, the electrochemical measurement for the sulfur oxidation reaction (SOR) was carried out in an H-type cell with a Nafion membrane (N-117, Dupont). The 1 M NaOH with and without 1 M Na_2S were used as the electrolytes in the anodic and cathodic compartment, respectively. Before the electrochemical measurement, all the working electrodes were subjected to cyclic voltammetry (CV) scanning from 0 to 0.9 V *vs*. RHE for 20 cycles at a scan rate of 50 mV s^{-1}. Linear sweep voltammetry (LSV) within the same potential window was recorded with a scan rate of 5 mV s^{-1} without *iR* compensation to obtain the polarization curves. Tafel slopes were derived by fitting the linear regions of the Tafel plots according to the equation $\eta = b\log(j) + a$.

The electrochemical double-layer capacitance (C_{dl}), which is proportional to the electrochemically active surface area (ECSA), was determined from CV curves measured in a non-Faradaic region (between 0.108 V and 0.208 V *vs*. RHE) at various scan rates (20, 30, 40, 50, and 60 mV s^{-1}). The C_{dl} value can be evaluated by analyzing the slope between $\Delta j/2$ at 0.158 V (*vs*. RHE) and the scan rate.

Electrochemical Impedance Spectroscopy (EIS) was carried out at open circuit potential with an AC amplitude of 5 mV over a frequency range of 10^6 to 10^{-2} Hz.

For the Faradaic Efficiency (FE) of the anodic SOR, constant-current electrolysis was performed in an H-type cell utilizing 1.0 M NaOH with 1.0 M Na_2S as the anolyte at an applied current density of 200 mA cm^{-2}. Upon completion of the electrolysis process, the total passed charge (Q) was recorded. The post-electrolysis anolyte was carefully collected and ice-cooled, followed by the dropwise addition of H_2SO_4 until reaching pH=1 to precipitate the oxidation product. The resulting yellow precipitate (S_8) was isolated via centrifugation, washed thoroughly with deionized water, dried at 60 ℃ for 24 h, and precisely weighed. The anodic FE was calculated using gravimetric analysis by comparing the actual mass of the collected sulphur to the theoretical mass derived from Faraday's law. For the cathodic HER， controlled electrolysis for HER was carried out in a sealed electrochemical cell containing 1.0 M NaOH at a constant cathodic current density of 100 mA cm^{-2}. The volume of the evolved H_2 gas was quantitatively monitored and collected in real-time using a calibrated water-displacement gas collection apparatus.

Long-term stability for SOR was assessed by continuous chronoamperometry at a constant potential of 0.4 V *vs*. RHE without *iR*-compensation, and the electrolyte was replenished every 20 hours. For

stability testing under full electrolysis conditions, a membrane electrode assembly (MEA) flow cell was used. Co_3O_4/NCS/NF electrodes with dimensions of 1.0 × 1.0 cm^2 were used as both the anode and cathode, with an Proton Exchange Membrane (Nafion 117) separating them. The MEA was then placed between Ti metal plate and Ni metal plate with parallel flow channels (1 mm wide × 0.5 mm deep) on both sides and sealed with silicone gaskets. The assembly was secured with eight stainless steel bolts, tightened using wrench in a crossed pattern. Prior to formal measurements, all fresh catalysts were activated via CV scanning until the electrocatalyst reached stability.

Harvest of sulfur product

After the SOR, H_2SO_4 was added dropwise to the ice-cooled electrolyte until pH 1. After centrifugation, the yellow precipitate was collected and dried at 60 °C for 24 h.

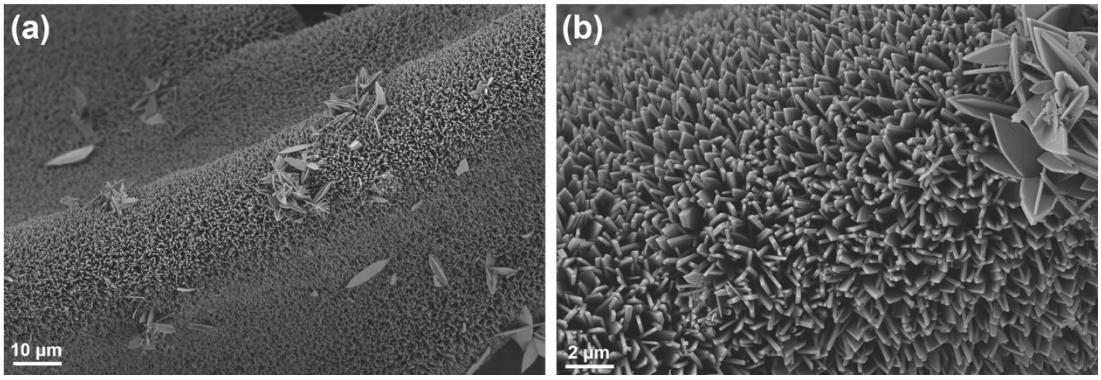

Fig. S1 SEM images of the Co-ZIF-L grown on NF at (a) high and (b) low magnifications, displaying a characteristic leaf-like morphology.

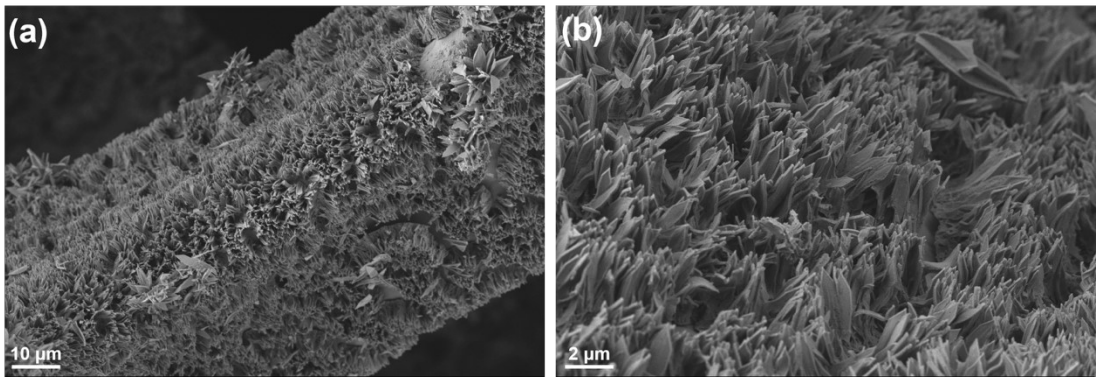

Fig. S2 SEM images of the porous Co_3O_4 nanosheet arrays obtained after calcination of Co-ZIF-L at 350 °C in air at (a) high and (b) low magnifications.

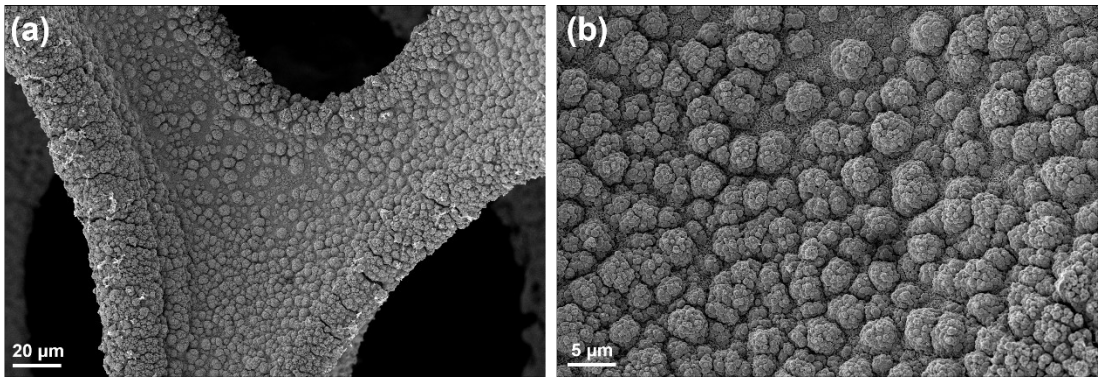

Fig. S3 SEM images of the control sample NCS/NF (without Co_3O_4 interlayer) at (a) high and (b) low magnifications, showing the morphology of nickel-cobalt sulfides directly electrodeposited on nickel foam.

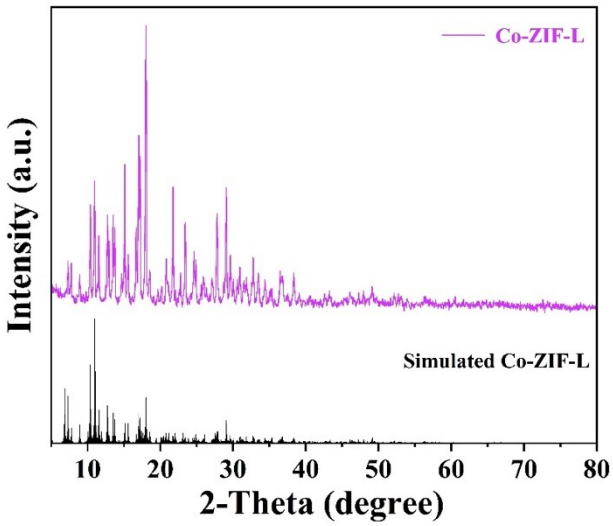

Fig. S4 XRD pattern of the as-synthesized Co-ZIF-L precursor, matching the simulated crystal structure of ZIF-L.

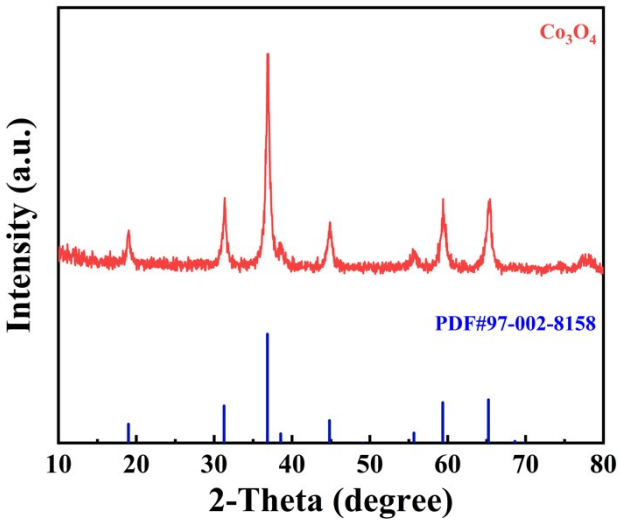

Fig. S5 XRD pattern of the Co_3O_4 product, indexed to the cubic spinel structure (JCPDS No. 97-002-8158).

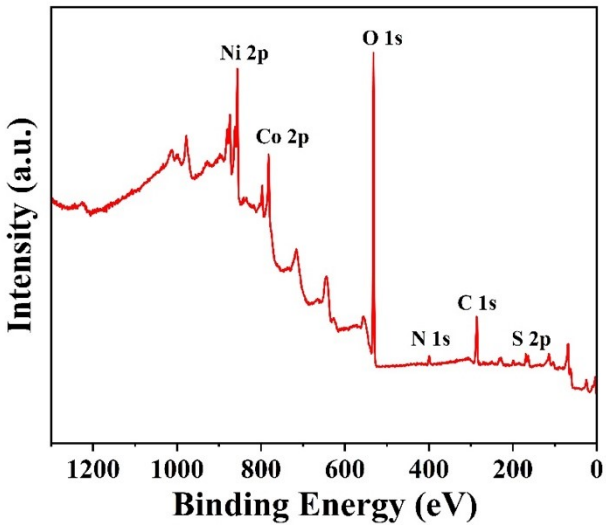

Fig. S6 XPS survey spectrum of the Co_3O_4/NCS/NF hybrid catalyst, confirming the coexistence of Co, Ni, S, O, and C elements on the surface.

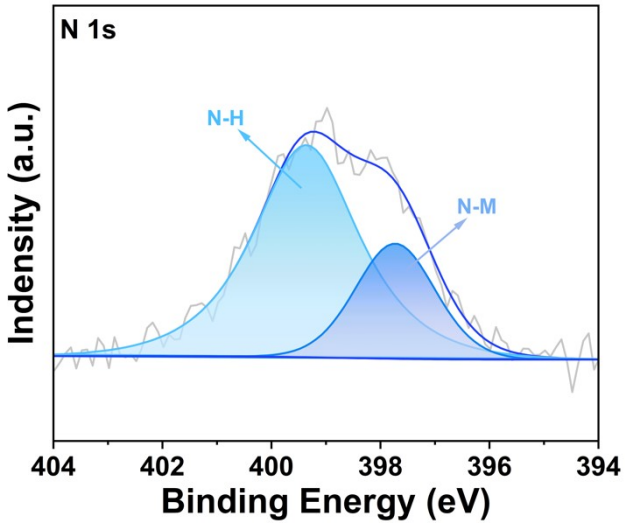

Fig. S7 High-resolution N 1*s* XPS spectra of Co_3O_4/NCS/NF.

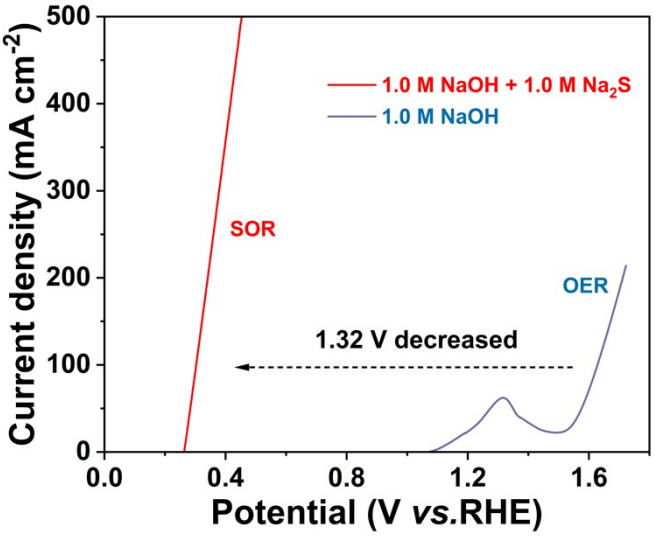

Fig. S8 LSV curves of the Co_3O_4/NCS electrode in 1 M NaOH with/without Na_2S.

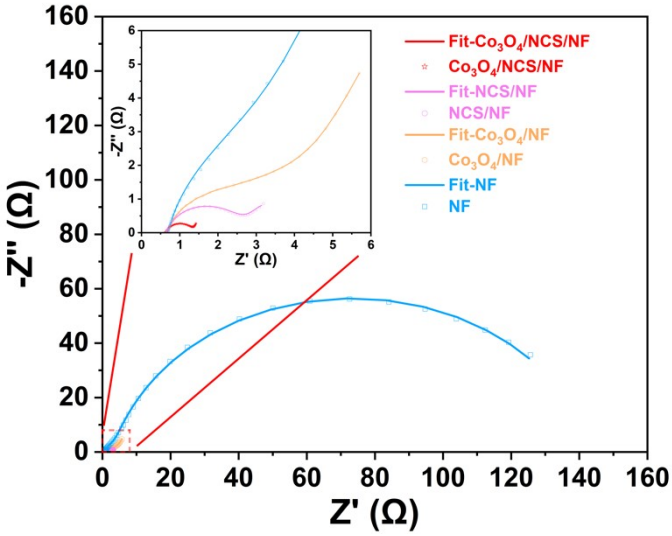

Fig. S9 EIS Nyquist plots.

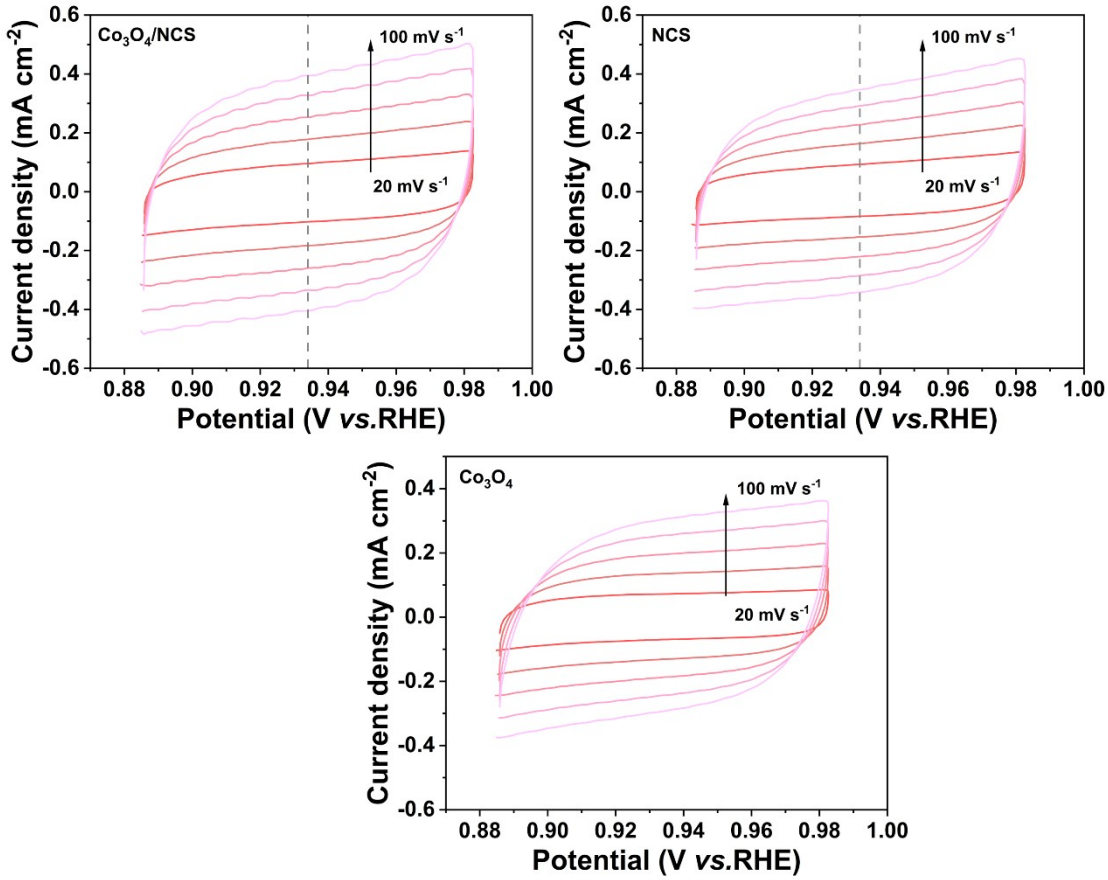

Fig. S10. CV curves of all tested catalysts at various scan rates in the non-Faradaic region.

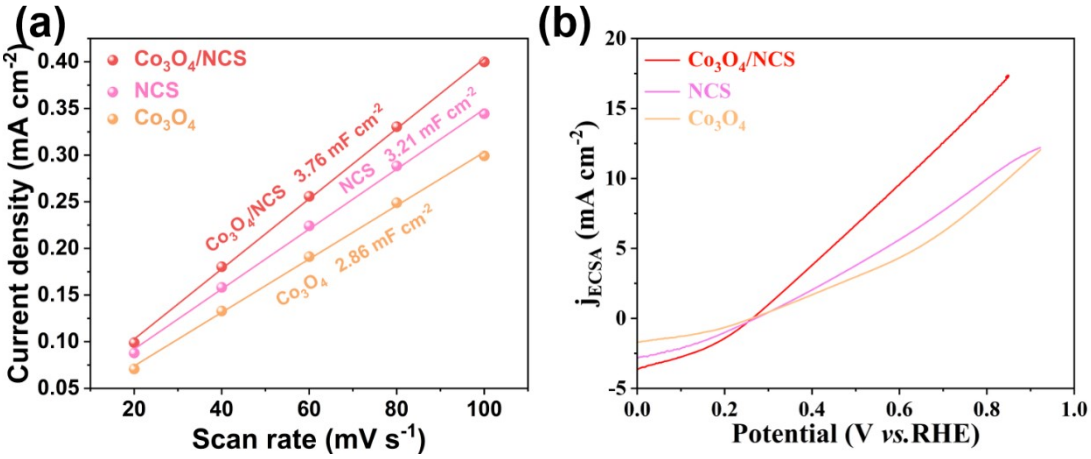

Fig. S11. (a) C_{dl} of catalysts derived from the current density versus the scan rate (b) ECSA-normalized LSV curves.

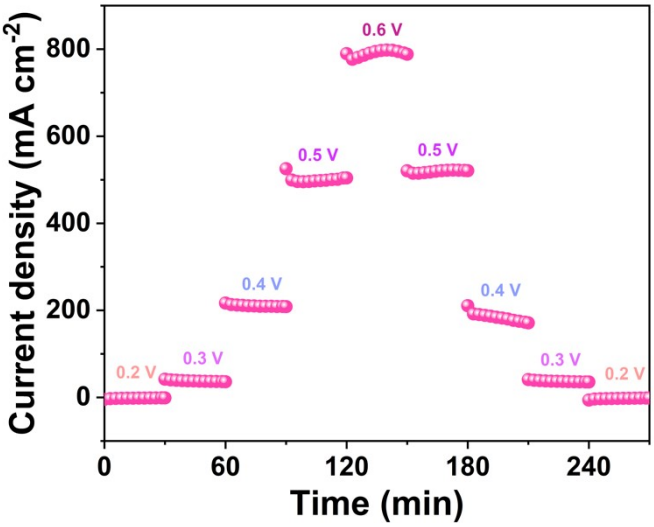

Fig. S12. Sequential chronoamperometric analysis of Co_3O_4/NCS for SOR

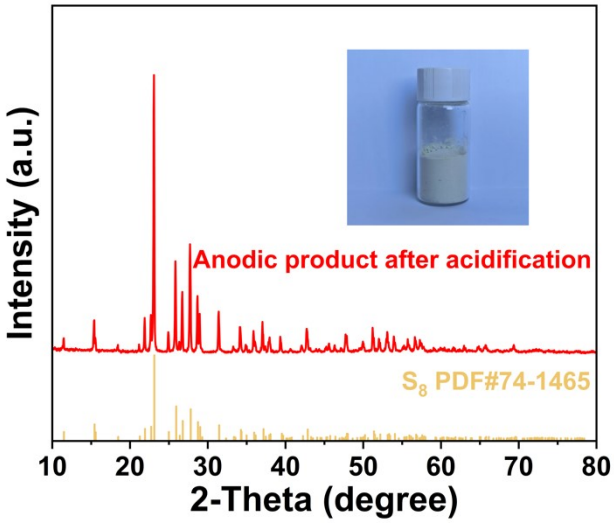

Fig. S13. XRD pattern of the collected sulfur product. Inset digital image exhibits the powder of collected sulfur product.

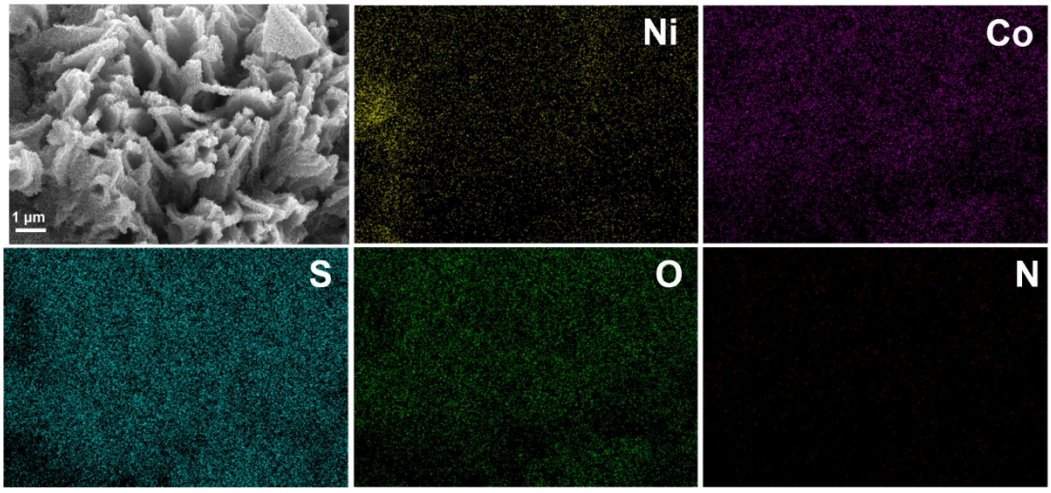

Fig. S14. FE-SEM images and Quantitative EDS analysis of Co_3O_4/NCS catalyst after 300-hour SOR stability test at 0.4 V vs. RHE.

Note 1.

To thoroughly understand the origin of this remarkable durability and the surface reconstruction mechanism during prolonged SOR, we performed comprehensive post-stability characterizations. Following 300 hours of continuous operation, post-mortem FE-SEM imaging confirms that the catalyst's hierarchical 3D network remains entirely intact, without structural collapse or the accumulation of bulk elemental sulphur.

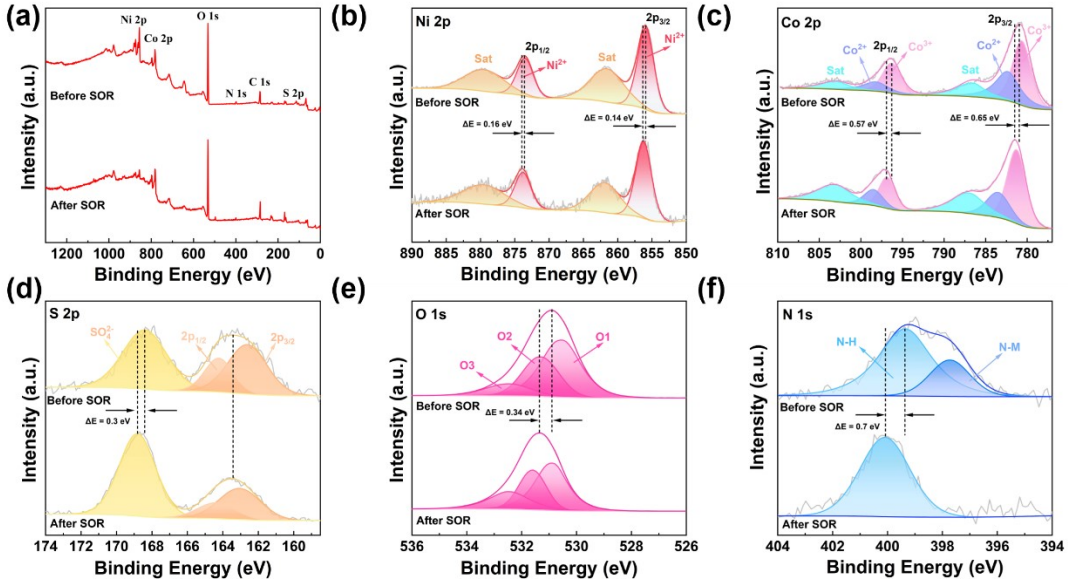

Fig. S15. (a) XPS survey spectrum of the Co_3O_4/NCS/NF before and after SOR (b) Ni 2*p*, (c) Co 2*p*, (d) S 2*p*, (e) O 1*s* and (f) N 1*s* XPS spectra of Co_3O_4/NCS/NF catalyst before and after SOR test.

Note 2.

High-resolution XPS analysis and quantitative energy-dispersive EDS (Table S2) reveal a mild, performance-enhancing surface reconstruction rather than degradation. High-resolution XPS characterization revealed a universal shift of the Ni 2*p*, Co 2*p*, S 2*p*, and O 1*s* spectra toward higher binding energies, indicating dynamic electron transfer from the Co_3O_4/NCS heterointerface to strongly adsorbed polysulphide intermediates. A portion of Co^{2+} is mildly oxidized to Co^{3+}. While the Ni^{2+} sites remain structurally stable. Crucially, the absence of insulating elemental sulphur signals in the post-stability S 2*p* spectrum validates that the ZIF-L-derived heterointerface effectively optimizes the adsorption-

activation capacity for intermediates, suppressing irreversible sulphur passivation and enabling ultra-stable operation.

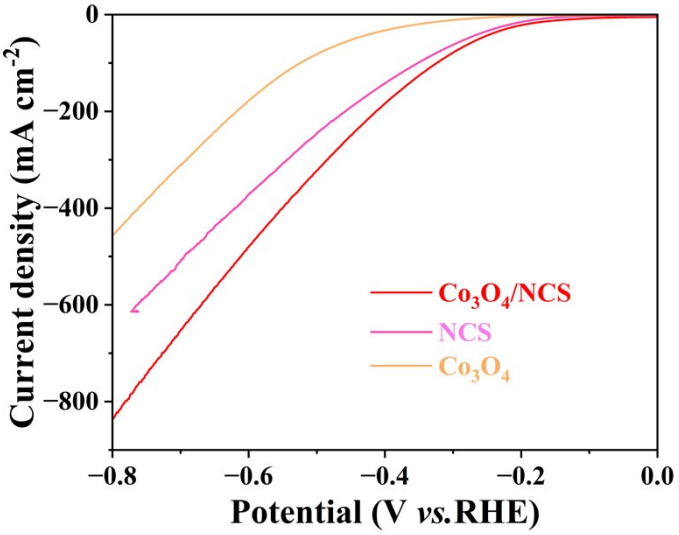

Fig. S16. Electrocatalytic performance for the hydrogen evolution reaction (HER) in 1 M NaOH.

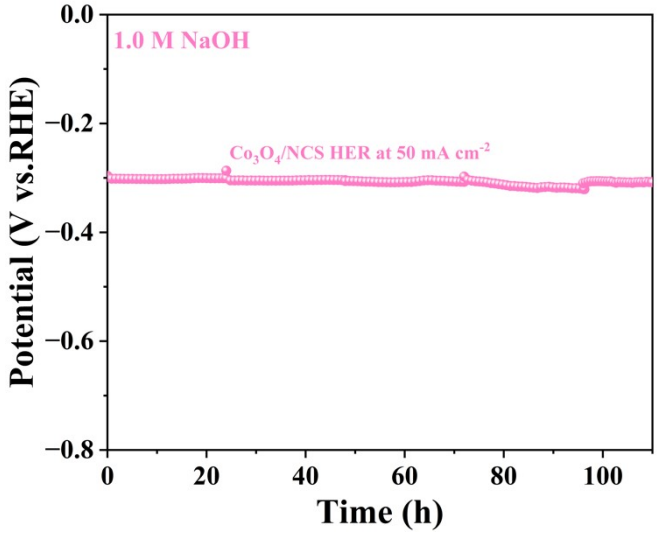

Figure S17. Long-term chronoamperometric stability test of Co_3O_4/NCS for the HER.

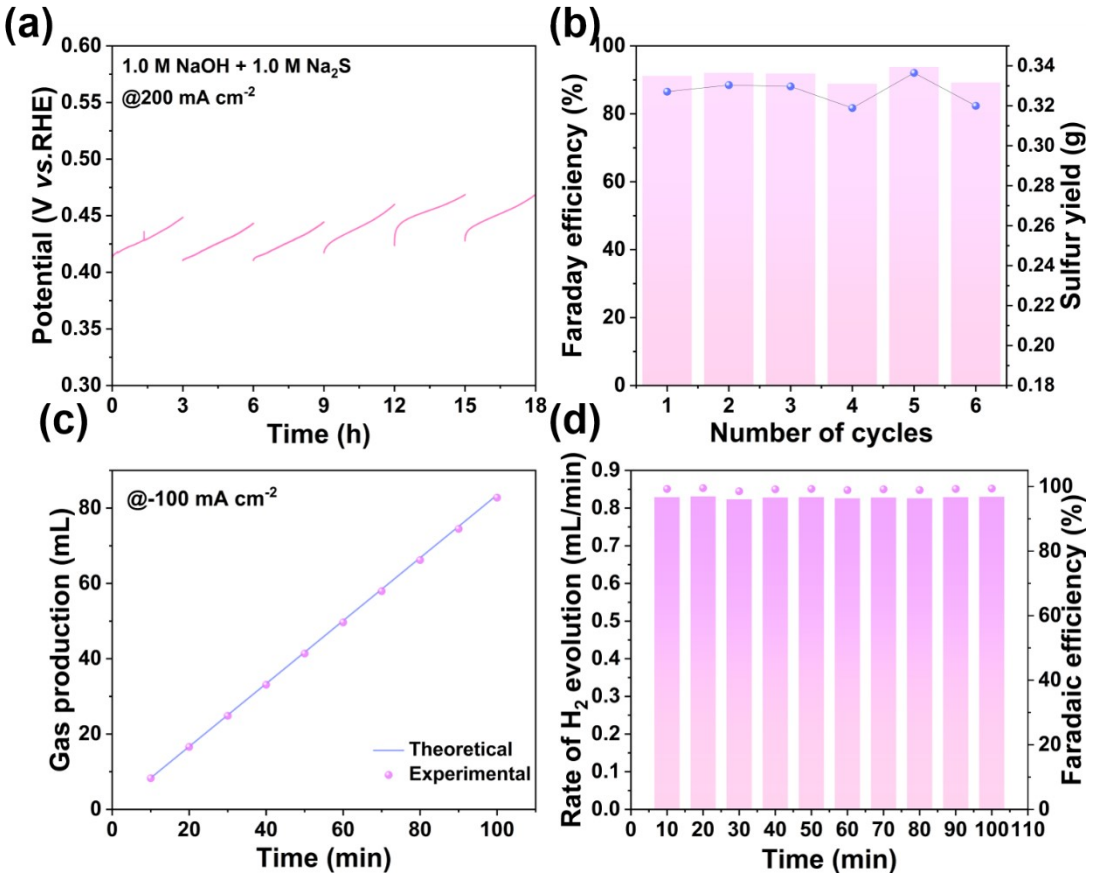

Figure S18. (a) 200 mA cm^{-2} constant current curve (electrolyte volume: 35 mL) (b) Sulfur powder yield and Faraday efficiency obtained from Fig.(a) (c-d) Faradaic efficiency for hydrogen production in 1.0 M NaOH

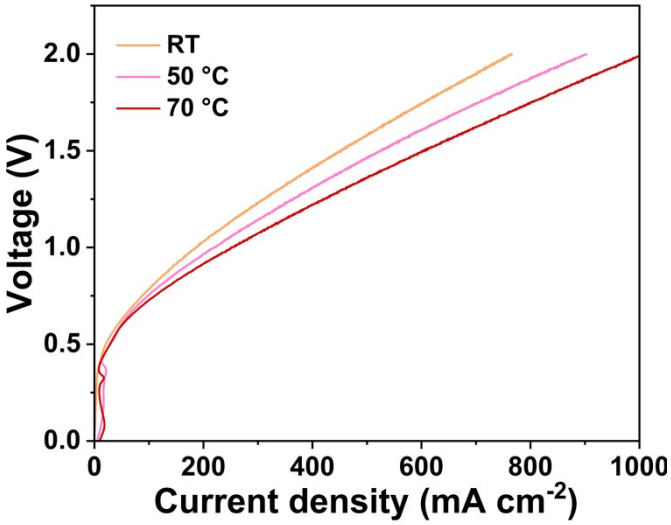

Figure S19. LSV curves at room temperature (RT) to 70 ℃.

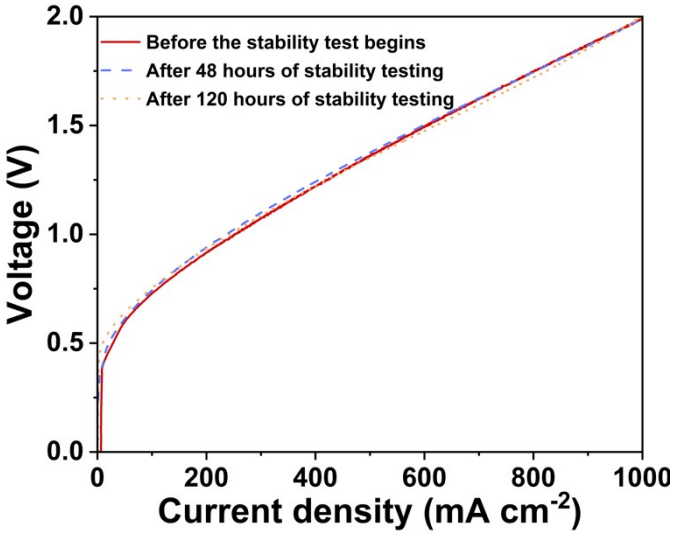

Figure S20. LSV curves before and after the stability test.

Table S1. Comparison of the current densities obtained at different potentials on various electrodes for SOR reactions.

Catalysts	Reaction conditions	Current density (mA cm^{-2}) @ E (V *vs*. RHE)	Stability	Ref.
Co_3O_4/NCS/NF	1.0 M NaOH + 1.0 M Na_2S	100 @ 0.303 500 @ 0.453	0.4 V vs. RHE @ 300 h	**This work**
Co_xP/NF	1.0 M KOH + 1.0 M Na_2S	100 @ 0.386	100 mA cm^{-2} @ 60 h	[S1]
V-N_3S_2-2/NF	1.0 M KOH + 1.0 M Na_2S	10 @ 0.283 100 @ 0.345	1.0 M KOH + 2.0 M Na_2S 10 mA cm^{-2} @ 240 h	[S2]
CoS_x/NF	1.0 M KOH + 1.0 Na_2S	100 @ 0.376	100 mA cm^{-2} @ 16 h	[S3]
Ag-Ni_3S_2/NF	1.0 M KOH + 1.0 M Na_2S	100 @ 0.314	100 mA cm^{-2} @ 80 h	[S4]
MoS_2/Co_8FeS_8/Ni_3S_2 /NF	1.0 M KOH + 1.0 M Na_2S	100 @ 0.353	0.266 V @ 50 h	[S5]
Fe-$Ni_{0.85}Se$/NF	1.0 M NaOH + 1.0 M Na_2S	10 @ 0.34 400 @ 0.593	10 mA cm^{-2} @ 20 h	[S6]
V-NiP/NF	1.0 M NaOH + 1.0 M Na_2S	10 @ 0.313 200 @ 0.52	200 mA cm^{-2} (cell) @ 100 h	[S7]
Co_3S_4/NF	1.0 M NaOH + 1.0 M Na_2S	100 @ 0.337	100 mA cm^{-2} @ 120 h	[S8]
MoO_2-Ni_3S_2/NF	1.0 M NaOH + 2.0 M Na_2S	100 @ 0.3	100 mA cm^{-2} @ 180 h	[S9]
MSN-350/NF	1.0 M NaOH	300 @ 0.46	0.4 V vs. RHE	[S10]

	+ 1.0 M H_2S		@ 100 h	
Fe-Ni_3S_2/NF-IS	1.0 M NaOH	100 @ 0.33	40~80 mA cm^{-2} @ 144 h	[S11]
	+ 1.0 M Na_2S			
$Ni(OH)_2/NiS_x$/NF	1.0 M NaOH	100 @ 0.315	100 mA cm^{-2} @ 48 h	[S12]
	seawater			
	+ 1.0 M Na_2S			

Table S2. EDS quantitative analysis of Co_3O_4/NCS catalyst before and after the 300-hour SOR stability test

Element	Fresh catalyst (a.t.%)	Post-stability catalyst (a.t.%)	Content change
Ni	10.55	12.91	+2.36
Co	28.42	23.84	-4.58
S	9.28	26.35	+17.07
O	48.37	35.97	-12.40
N	3.37	0.93	-2.44

Reference.

S1. H. Chen, M. Xiong, S. Qiao, S. Wu, C. Rao, G. Luo, L. Wang, S. Ci and Z. Wen, Chem. Eng. J., 2025, 524, 169400.

S2. S. Liu, Y. Gu, J. Kang, J. Zhang, S. Liu, H. Yang, X. Zhu and M. Ming, Int. J. Hydrogen Energy, 2026, 198, 152670.

S3. B. Tang, K. Jiang, W. Yin, W. Xing, J. Zhang, S. Pi, J. Liang, L. Tang and W. Tang, Small, 2025, 21, e08173.

S4. M. Ming, J. Kang, Y. Gu, J. Zhang, Q. Zhang, G. Fan and Q. Shen, Environ. Chem. Eng., 2025, 13, 119139.

S5. W. Zhao, H. Zhou, L. Liu, Y. Wang, S. Li, L. Guo, E. Liu, Z. Zhang and T. Sun, Adv. Funct. Mater., 2025, e19053.

S6. S. Xie, X. Wang, Y. Li, S. Liu, J. Qian, Y. Zhang, L. Jiang, Z. Cao, Z. Yan, X. Wan, Z. Yang, L. Zou, W. Zhang and R.-Q. Li, Chem. Sci., 2025, 16, 12587-12593.

S7. R.-Q. Li, X. Wang, S. Xie, S. Guo, Z. Cao, Z. Yan, W. Zhang and X. Wan, Chem. Sci., 2025, 16, 809-815.

S8. C. Zhang, X. Wang, J. Jiang, J. Zhang, A. Liu and L. Ai, Appl. Catal. B Environ, 2025, 365, 124991.

S9. L. Hao, M. Wang, J. Lei, Z. Chen, Z. Wang and Y. Deng, Appl. Surf. Sci., 2026, 725, 165841.

S10. N. Sinha, C. Das, S. Pal and P. Roy, ACS Appl. Energy Mater., 2025, 8, 13631-13644.

S11. X. Hao, X. Che, C. Liu, Q. Yang, Y. Liu, G. Liu, Y. Yang, Q. Huang and P. Gu, Fuel, 2026, 417, 138588.

S12. H. Li, L. Zhang, W. Liu, T. Gui, L. Xiao, Q. Liu, J. Ding, G. Hu and X. Liu, Mater. Chem. Front., 2025, 9, 2658-2667.